Competitive Electrohydrodynamic and Electrosolutal Advection Arrests Evaporation Kinetics of Droplets

Vivek Jaiswal, Shubham Singh, Anilakkad Raman Harikrishnan, and Purbarun Dhar*

Read Online

ACCESS | Metrics & More | Article Recommendations

ABSTRACT: This article reports the hitherto unreported phenomenon of arrested evaporation dynamics in pendant droplets because of electric field stimulus. The evaporation kinetics of pendant droplets of electrically conducting saline solutions in the presence of a transverse, alternating electric field is investigated experimentally. While the increase of field strength reduces the evaporation rate, increment in field frequency has the opposite effect. The same has been explained on the solvation kinetics of ions in polar water. Theoretical analysis reveals that change in surface tension and the diffusion-driven evaporation model cannot predict the decelerated evaporation. With the aid of particle image velocimetry, suppression of internal circulation velocity within the droplet is observed under electric field stimulus, which directly affects the evaporation rate. A mathematical scaling model is proposed to quantify the effects of electrohydrodynamic circulation and electrothermal and electrosolutal advection on the evaporation kinetics. The analysis encompasses major governing parameters, namely, the thermal and solutal Marangoni numbers, the electrohydrodynamic number, the electro-Prandtl and electro-Schmidt numbers, and their respective contributions. It has been shown that the electrothermal Marangoni effect is suppressed by the electric field, leading to deteriorated evaporation rates. Additionally, the electrosolutal Marangoni effect further suppresses the internal advection, further reducing the evaporation rate by a larger proportion. Stability analysis reveals that the electric body force retards the stable internal advection. The stability mapping also illustrates that if the field strength is high enough for the electrosolutal advection to overshadow the solutal Marangoni effect completely, it can lead to improvement in evaporation rates.
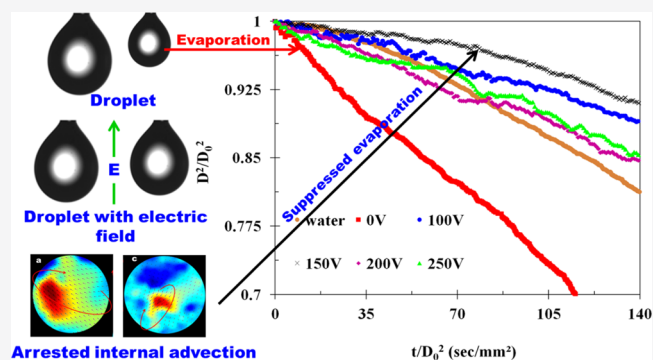
INTRODUCTION

Hydrodynamics and thermal and species transport phenomena in microscale droplets and sprays have garnered research interest for quite some time because of evolution and advancement of systems involving droplets. The range of applications of droplets has triggered the recent research and development activities. The major utilities are in biomedical devices (spray medications, DNA patterning, pathological tests, nebulizers, inhalers, etc.), internal combustion engines,[1−3] thermal treatment,[4] printing technology, and the Heating, Ventilation, Refrigeration and Air Conditioning (HVRAC) sector. Insecticides, fertilizer sprays and repellents,[5,6] lab-on-chip devices, and droplet-based sorting microfluidic devices are other applications where droplet dynamics play important roles. There are two droplet shapes in general, the sessile and the pendant. The major focus of studies on droplet dynamics has been on sessile droplets, where the attention has primarily been on the interfacial properties. Reports by Picknett and Bexon,[7] Hu and Larsen,[4] Kaushal et al.,[8] Semenov et al.,[9] and so forth are some examples of studies on sessile droplet evaporation. Godsave[10] considered a spherical droplet evaporating in a quasistatic gas phase with

a constant diffusion rate and reported the classical D^2 law as a pioneering literature on pendant droplet evaporation. Further models[11] incorporate the ambient pressure conditions with the D^2 law. Recent developments in pendant droplets involve multiphysics phenomena, such as manipulation by an electromagnetic field.[12] Solvated solutes also morph the fluid dynamics and thermospecies transport in the droplets, and such characteristics have been reported.[13,14]

Electrohydrodynamics has shown promise in microfluidic applications such as patterning, flow actuation, separation, and control. The shape of a pendant droplet is governed by surface tension, and electric fields can change the shape and wetting dynamics of droplets. Studies have reported the physics of droplet deformation and fluid dynamics under the effect of an
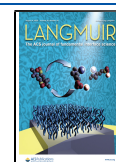
electric field.[15−20] Such studies numerically construct the best fit for the deviation of the axisymmetric droplet because of the electric field and combine the Laplace, Young−Laplace, Maxwell, and Stokes deformation fields to determine the droplet morphology.[21] The electric field also exerts a body force, which could result in the Coulomb force, dielectrophoretic (DEP) force, and electrostriction components. The Coulomb force arises because of the interaction of free, charged particles with the fluid, whereas DEP streaming and electrostriction force arise out of a nonuniform electric field and dielectric permittivity mismatch. The strain generated by the field can lead to electropropulsion, electro-Leidenfrost effect, and electrowetting of droplets.[22−24] The electro-Leidenfrost effect[25] is caused by a decrease in vapor layer thickness with increasing field strength across the substrate. Reports also discuss droplet propulsion under the influence of an alternating electric field,[26] rhythmic oscillation,[27] electro-generation of emulsion,[28] electrocoalescence,[29] and living cell manipulation with electro-microhydrodynamics.[30]

A survey of droplet electrohydrodynamics shows that the major focus has been on droplets dispersed in another liquid medium. It has also been seen that the interfacial and internal hydrodynamics of the droplet can be modulated by application of electric fields. It has been shown by the authors that the presence of solvated ions in a pendant droplet leads to augmented evaporation dynamics.[14] The augmentation is caused by the internal advection within the droplet, which is generated by thermosolutal gradients. The role of solutal Marangoni and its dominance over thermal Marangoni was also reported. Drawing inspiration from the study, the influence of internal electrohydrodynamics on droplet evaporation kinetics is investigated in the current article. The solvated ions within the droplet constitute an electrically conducting system, which is expected to respond to an electric field stimulus. The electric body force is expected to lead to changes in the internal advection patterns, which would consequently lead to changes in the evaporation dynamics of the pendant droplet. Experimental determination of the evaporation rate at variant salt concentrations, electric field strengths, and frequencies has been performed. Flow visualization to quantify the internal advection has been achieved using particle image velocimetry (PIV). Theoretical modeling of the evaporation kinetics shows that the electrohydrodynamic and electrosolutal transport exhibits competitive roles, which modulate the overall evaporation behavior. It is shown using experiments and theoretical scaling that droplet evaporation rates can be decelerated by the use of electric fields.

MATERIALS AND METHODOLOGIES

A customized experimental setup has been used for the study (schematic in Figure 1). The droplet is suspended from a steel needle using a digitally controlled precision dispensing mechanism (Holmarc Opto-Mechatronics Pvt. Ltd., India). A glass syringe of $50 \pm 0.1~\mu L$ capacity has been used, and a droplet of $20 \pm 0.5~\mu L$ volume was suspended as a pendant. The diameter of the droplet lies in the range of 2.8 ± 0.1 mm. Two electrodes have been arranged to apply the electric field across the droplet in a vertical orientation. The field was generated by the use of a programmable ac power supply (Aplab, India) (rated 50−500 Hz at 0.1 Hz resolution and 0−270 V at 0.1 V resolution). One terminal of the supply was connected to the steel needle, which acted as one electrode. The other terminal was connected to a steel sheet electrode placed below the hanging droplet (at a distance of 1 mm from the droplet bottom). This arrangement of
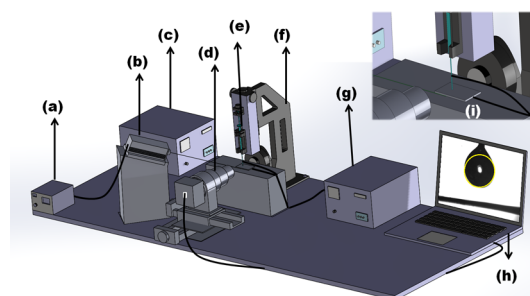
Figure 1. Schematic of the experimental setup, comprising a (a) laser controller, (b) laser mounted on a stand, with cylindrical lens for light sheet (not illustrated) (c) droplet dispenser and backlight controller module, (d) CCD camera with a two-axis movable stand and mounted with a microscopic lens assembly, (e) sterile glass syringe, (f) droplet dispensing mechanism, (g) programmable ac power source, and (h) data acquisition computer (the yellow circle is the region of interest of the droplet for the PIV analysis). Inset (i) illustrates a zoomed-in view of the arrangement of electrodes and the needle. The whole setup is housed within an acrylic chamber and mounted on a vibration-free table top.

field application has been illustrated in the inset of Figure 1. The distance between the needle electrode and the plate electrode was maintained at 3.5 mm. Four electric field strengths (100, 150, 200, and 250 V) and three frequencies (50, 100, and 200 Hz) have been used. In all the present experiments, sinusoidal waveform alternating field has been employed.

The case of pure water was compared to literature reports[14,31] to validate the experimental setup. The pure water is tested under the influence of different frequencies and field strengths and insignificant deviation was observed from the zero-field case. Two salts solutions (Table 1) of NaI (sodium iodide) and $CuSO_4 \cdot 5H_2O$ (copper sulfate

Table 1. Representative Property Values of Experimental Test Fluids

fluid	property	value
DI water	viscosity (mPa s)	0.92
	surface tension (mN/m)	72.3
0.1 M NaI	viscosity (Pa s)	1.09
	surface tension (mN/m)	75.6
0.2 M NaI	viscosity (Pa s)	1.36
	surface tension (mN/m)	81.8
0.1 M CuSO₄	viscosity (Pa s)	1.03
	surface tension (mN/m)	73.9
0.2 M CuSO₄	viscosity (Pa s)	1.17
	surface tension (mN/m)	77.2

pentahydrate) were used. Both the salts were procured from Sigma-Aldrich, India, and were chosen based upon findings reported by the present authors.[14] The evaporation process is recorded using a monochrome charge-coupled device (CCD) camera attached to a long-distance microscopic lens (Holmarc Opto-Mechatronics, India). The recording is done at 10 fps and a resolution of 1280×960 pixels. An intensity-controlled LED backlighting arrangement (DpLED, Japan) is employed as the light source. The ambient temperature and humidity are noted using a digital thermometer and hygrometer. The temperature and humidity range from $25 \pm 2~°C$ and $54 \pm 3\%$, respectively, at a location of 3 cm away from the droplet. The whole setup is housed within an acrylic chamber to isolate it from atmospheric influences. Thermal images of the droplet were recorded using an infrared camera (FLIR Technologies) having a sensitivity of 0.05 K and resolution of 640×480 pixels.

The image processing is done in the open source software ImageJ. Each instantaneous droplet image was fit to the closest pendant drop

shape, and the equivalent diameter was obtained from the drop shape analysis. PIV was done to quantify and visualize the flow patterns within the droplet. The salt solution was seeded with neutrally buoyant fluorescent particles (polystyrene, ~10 μm, Cospheric LLC, USA). For the PIV studies, a continuous wave laser (Roithner GmbH, Germany, 532 nm wavelength, 10 mW peak power) is used as the illumination source. A cylindrical lens is used to generate a laser sheet (~0.5 mm thickness) to illuminate the midplane of the droplet. PIV is performed during the initial stages of evaporation (within first 5 min) so that artifacts from the evaporation-induced change in the salt concentration are not appreciable. The PIV is done at 30 fps, and a resolution of ~120 pixels/mm is ensured. Postprocessing is performed using the open source code PIVLab. The region of interest for the PIV analysis has been shown in Figure 1h using a yellow circle. A standard cross-correlation algorithm with four pass interrogation windows of 64, 32, 16, and 8 pixels has been used. A stack of 800 images is investigated for maximizing the signal-to-noise ratio in the data and spatially averaged velocity contours and fields are obtained.
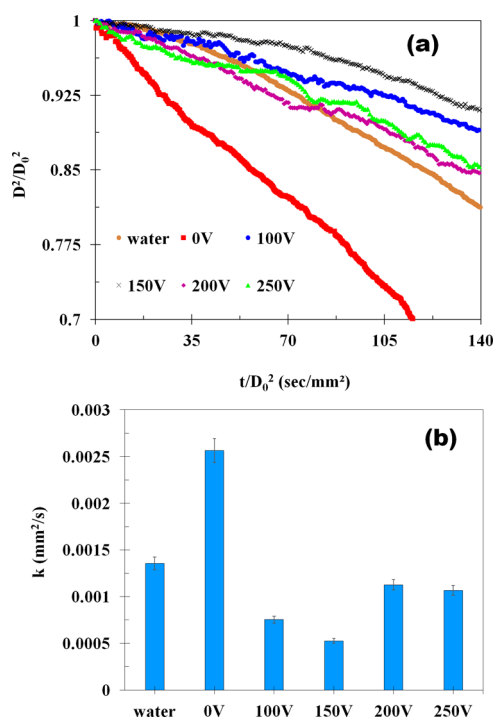
■ RESULTS AND DISCUSSION

Evaporation Kinetics in the Presence of an Electric Field. First, the evaporation kinetics of water and saline solutions are studied as control in the absence and presence of an electric field. It is noted that the evaporation rate of water droplets is the same for the field as well as zero-field case. Hence, in all figures, we only represent the 0 V case of water. Next, the evaporation characteristics of the saline droplets under variant field strengths and frequencies are studied. Figure 2a illustrates the evaporation behavior of water and 0.1 M NaI solution for an electric field of 50 Hz and different strengths. The evaporation kinetics of the saline droplets under the influence of an electric field is observed to conform to the classical D^2 law,[10] expressible as
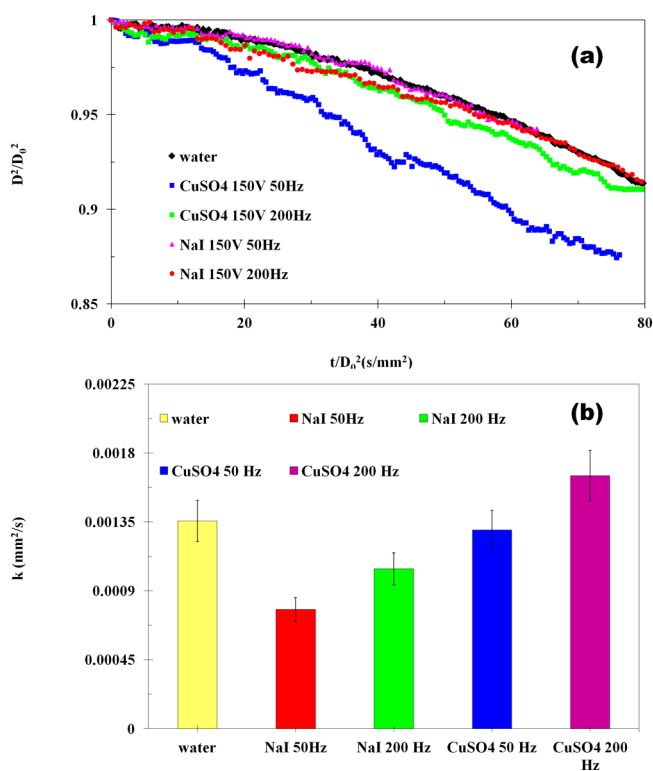
$$\frac{D(t)^2}{D_0^2} = 1 - k\frac{t}{D_0^2} \tag{1}$$

where $D(t)$, D_0, t, and k represent the instantaneous and initial diameter of the droplet, the elapsed time, and the evaporation rate constant, respectively. The slope of the best-fit straight line of the curves (Figure 2a) yields the evaporation rate constant, in accordance with eq 1. The fitting of the data points to eq 1 is done for the entire droplet lifetime in each case. The agreement of D^2 law with the data sets conforms to 0.92−0.98 goodness of fit. It is evident from Figure 2a that the addition of salt enhances the evaporation rate of the water. This enhancement is due to the solute-thermal advection within the droplet and is reported in the literature.[14]

With the electric field, the evaporation rate is observed to decrease drastically and deteriorates even below the rate of evaporation of pure water. However, at higher field strengths, the evaporation enhances by a small degree but is still below the rate of water or equivalent. Figure 2b illustrates the evaporation rate for the cases corresponding to Figure 2a. Figure 3a compares the evaporation rates for two salt (NaI and

Figure 3. (a) Evaporation rate of different salt solutions (0.2 M) at 150 V and for different field frequencies. (b) Evaporation rate constants corresponding to a frequency variation at 250 V. The water case is at 0 V.

Figure 2. (a) Evaporation dynamics of NaI solution (0.1 M) at 50 Hz and different field strengths. (b) Evaporation rate constant corresponding to field strength variation. The water case is noted to be same at all voltages studied and hence corresponds to 0 V in the figure.

$CuSO_4 \cdot 5H_2O$) solutions at the same concentration (0.2 M) for 50 and 200 Hz frequency at 150 V. For comparison, the case of pure water has also been illustrated. The figure shows two comparisons, one for change in frequency and the other for the nature of the salt solution, and Figure 3b illustrates the evaporation rates for cases corresponding to a field strength of 250 V. With increase in field strength, the values of evaporation which were closer to the water case are further reduced. It is observable that the evaporation of $CuSO_4$ is at times faster

compared to NaI, and this is already discussed in the previous report by the authors[14] and in earlier literature[32] (caused by the hydrated state and solvation thermodynamics of $CuSO_4$). It is observed from Figure 3b that increase in the field frequency leads to improved evaporation rates, whereas an increase in field strength leads to deteriorated evaporation (Figure 2).

This observation is further clarified later from Figure 5. The decrease in evaporation rate in the presence of an electric field may be explained based on ionic interactions within the polar fluid with an increase in field strength. In a strong polar fluid such as water, the solvated ions form weak physical bonds with the polar water molecules, with the cations partially attracted to the partly polar hydrogen of water and the anions to the oxygen. The solvated ions respond to the electric field, and the electrostatic force on the solvated ions increases with increment in potential difference across the electrodes. This additional body force on the solvated ions strengthens the weak physical bonds with the polar water molecules,[33] thereby increasing the threshold energy required by the water molecules at the droplet–air interface to diffuse away from the droplet, thereby decelerating the evaporation rate. The frequency of the field, on the other hand, determines the ionic migration propensity of the ions. At higher frequencies, the field polarity reverses at faster rates, which causes the solvated ions to fluctuate about their mean positions at higher frequencies in addition to the thermal fluctuations within the system. This increased field-induced fluctuation leads to weakening of the physical bonds with the polar water molecules, which eases the probability of the molecules at the interface to diffuse into the air phase, thereby improving the evaporation rate.

Role of Surface Tension on Evaporation in an Electric Field Ambiance. The change in the surface tension of the fluid can determine the change in the evaporative rate from the droplet. The surface tension of the droplet is measured using the pendant drop method under variant field conditions. Figure 4 illustrates the response of surface tension to stimuli of changing field strength (at the constant frequency) and changing frequency (at the constant field strength). The surface tension of pure water is noted as 72.5 mN/m and that of the 0.2 M NaI solution is observed as 82 mN/m, which is
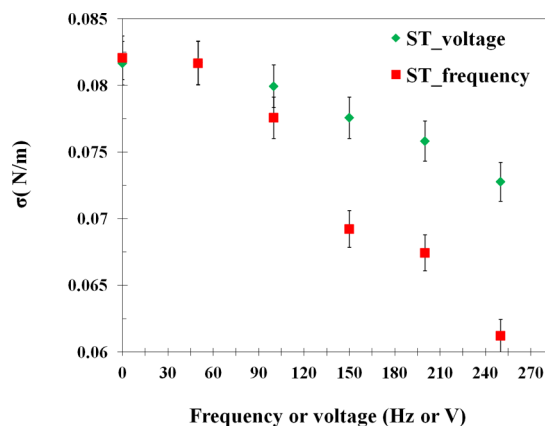
consistent with reports on salt solutions.[14] With the increase in field strength, the variation in surface tension ranges from 82 to 77 mN/m, whereas, for increase in field frequency, the variation ranges from 82 to 62 mN/m. Additionally, the decrease in case of field strength is gradual, whereas for frequency the descent is steeper. The point to note is that increase in both field strength and frequency leads to decrease in the surface tension value. This signifies that evaporation rates should be augmented because of a reduction in threshold surface energy for the departing water molecules. Whereas this partially explains the improvement in evaporation rates with increase in frequency, it fails to explain the deteriorated evaporation rates upon the increase of field strength. Thereby, additional probing is essential to establish the mechanism at play.

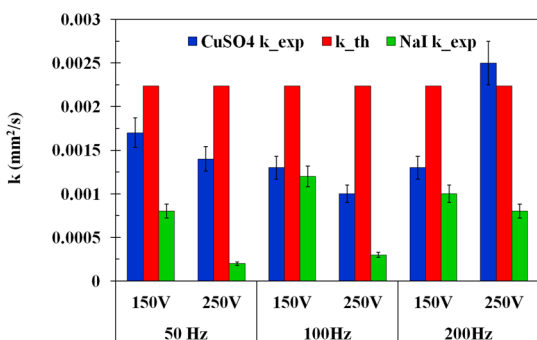**Contribution of Diffusion-Dominated Evaporation.** As multiple mechanisms could be involved in modulating the evaporation, a sequential discussion on each mechanism will provide clarity regarding their contributions. The mechanism by which a pendant droplet evaporates is molecular diffusion. Consequently, the diffusion-driven evaporation model[3] is appealed to. The approach considers a thin film of vapor formed on the surface of the droplet by the escaping water molecules, from which the vapor further escapes to the ambient by a concentration gradient. The evaporation is assumed as quasisteady, and the thermal and mass transport is only through the diffusion film. Applying the equation of conservation with uniform droplet temperature and the temperature and vapor concentration of the diffusion layer outside the droplet as boundary conditions, the evaporation rate is expressed by eqs 2 and 3 as[3]

$$B_M = \frac{Y_s - Y_\infty}{1 - Y_s} \tag{2}$$

$$\frac{dm}{dt} = 2\pi \rho_g D_v R \ln(1 + B_M) Sh \tag{3}$$

In eqs 2 and 3, dm/dt is the droplet evaporation rate, D_v is the diffusion coefficient of the vapor with respect to the ambient phase, ρ_g is the density of the ambient gas, R is the droplet radius, and λ is thermal conductivity of the ambient gas phase. Sh and B_M are the Sherwood number and Spalding mass number, respectively. Y_s and Y_∞ are the mass fractions of the vapor at the droplet surface and in the ambient phase. It has been shown[34] that the diffusion-driven evaporation is not perturbed because of the miniscule changes in Henry's constant of the system due to the presence of such dilute quantities of salt. Figure 5 illustrates the comparison of the diffusion model predictions with experimental evaporation rate constants. It is observed that the model cannot predict the evaporation rates under different field constraints. However, it may be noted that the model is able to predict the evaporation rate for the pure water case (not illustrated). This observation is justified as the diffusion-driven model only considered phenomena across the vapor diffusion layer and does not encompass mechanisms within the droplet or at the interface. Thereby, it is evident that the internal and interfacial dynamics need to be accounted for in explaining the diminished evaporation kinetics.

Internal Advection Dynamics under an Electric Field Stimulus. Internal advection within droplets, caused by thermal and/or solutal gradients, can majorly affect changes in evaporation rates. The advection within the droplet and on

Figure 4. Variation of surface tension with a change in the voltage (indicated as ST_voltage) and frequency (indicated as ST_frequency) for 0.2 M NaI solution. The extreme limits of change in the surface tension have been illustrated.

Figure 5. Comparison of experimental evaporation rate with the diffusion-driven theoretical approach.[3] The diffusion-driven model fails to predict experimental evaporation dynamics.

the droplet interface generates shear within the shrouding diffusion layer. This leads to replenishment of the diffusion layer with ambient gas, which enhances the concentration gradient and improves evaporation.[14,31,35] The internal advection is qualitatively and quantitatively determined by PIV for the water and 0.2 M saline droplets. These studies were done within the initial 5 min of evaporation to avoid the effects of change in the concentration of the solution on the internal advection dynamics. The internal circulation dynamics for water and saline droplet in zero-field environment conforms with literature reports.[14,31,35] The water droplet shows no change in advection dynamics in the field environment. Figure 6 illustrates the time-averaged velocity
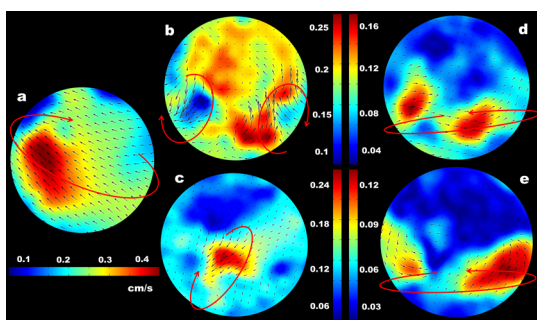

Figure 6. Internal circulation velocity contours and time-averaged flow field for (a) 0 V, (b) 50 Hz, 100 V (c) 50 Hz, 250 V (d) 200 Hz, 100 V, and (e) 200 Hz, 250 V, respectively. The concentration of NaI is 0.2 M for all cases. The large red arrows indicate the spatially dominant direction of advection.

contours and fields (for 800 subsequent velocity fields) for different field strengths and frequencies. Figure 6a shows that the 0.2 M NaI under zero-field conditions exhibits a major advection cell within the entire bulk of the droplet. When the field strength increases (Figure 6b,c), the circulation changes the orientation to an orthogonal plane, and two opposing vortices form near the bulb of the pendant at 100 V along with a suppression in velocity. At 250 V, the velocity is further reduced, and a single small circulation cell operates at the bulb of the pendant. In fact, at 250 V, the spatially averaged velocity is similar to the drift noted within water droplets,[31,35] except for the region of circulation near the bulb.

For increase in frequency (Figure 6b,d), it is observed that the pattern of advection regains similarities with the zero-field case, albeit with the circulation region smaller in size than the zero-field case. Additionally, the velocity magnitude, although

less than the zero-field saline case, is relatively greater than the high field strength case. Figure 6a–d reveals that the field strength has a dominating role in the apprehension of internal circulation in comparison to field frequency. However, unlike high field strength cases, high-frequency cases lead to reduction in the internal circulation velocity, but without major changes in the advection patterns. As observable from Figure 6d,e, at high frequencies, the internal circulation is very similar to the zero-field case. However, the major portion of advection is confined toward the bulb of the droplet. This behavior is due to the nature of the field imposed. Whereas the bottom electrode is of a plate type, the top electrode is the needle itself. Thereby, the field lines diverge from the tip of the needle and spread onto the bottom electrode. The field lines influence the neck of the pendant to a lesser extent than the bulb, which is possibly the reason why internal advection dynamics are concentrated toward the bulb in all field conditions.

Visualization reveals that the electric field decelerates the advection, which in turn reduces the evaporation rate of the saline solution. Figure 7a illustrates the temporal spectrum of
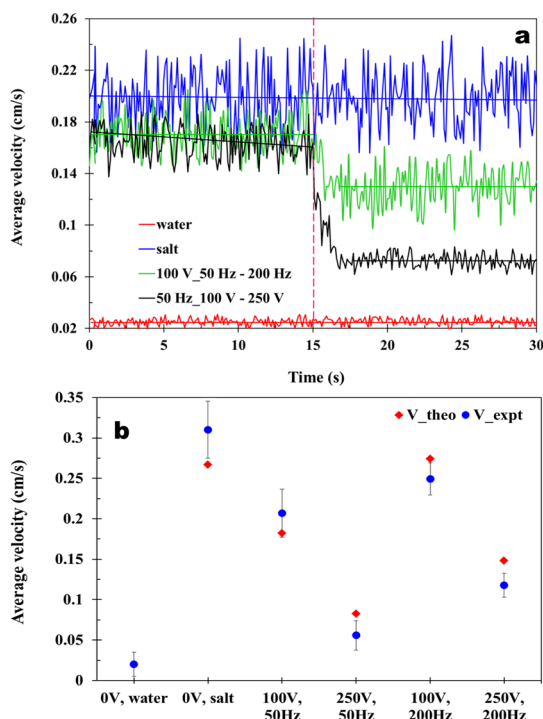
Figure 7. (a) Transient variation of the spatially averaged circulation velocity for water and 0.2 M NaI salt solution droplets under variant field parameters. The lines illustrate the best-fit average velocity. (b) Comparison of the theoretical velocities from the scaling model concerning the spatially averaged with the experimentally determined velocities.

the spatially averaged instantaneous velocities under different field constraints. The water case shows a minor drift, whereas the zero-field salt case exhibits largely augmented circulation, with large-scale temporal fluctuations in the average velocity. This corroborates with reports for saline or binary fluid systems.[14,31,35] In one case, the field at 50 Hz and 100 V has been applied for the first 15 s, and then, the field frequency is increased to 200 Hz. In another case, initially 50 Hz and 100 V are applied, and after 15 s the field strength is increased to 250
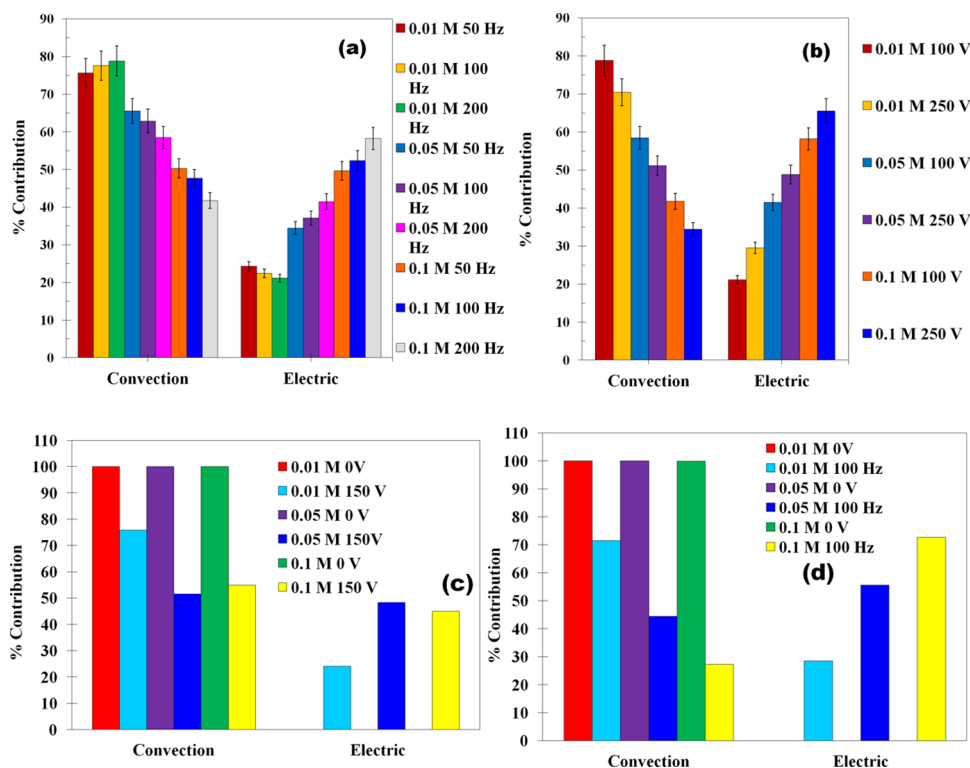
Figure 8. Contribution of different mechanisms in thermal transport with (a) frequency variation at 150 V and (b) field strength variation at 100 Hz and in species transport with (c) field strength variation at 100 Hz and (d) frequency variation at 150 V.

V. It is observed that initially both cases exhibit similar spectra as the field strength and frequency are the same. When the field is increased suddenly at 15 s from 100 to 250 V, a reduction in the spatially averaged velocity is noted, with the average velocity reducing by ∼70% of the original. However, when the frequency is increased from 50 to 200 Hz, the reduction in the velocity is ∼25%. Additionally, it is observed that the higher field strength also dampens out the temporal fluctuations largely compared to the higher frequency case. At higher frequencies, the electrophoretic motion of the solvated ions exhibit field-influenced fluctuations, which lead to local hydrodynamic fluctuations, thereby leading to augmented temporal velocity fluctuations. The higher field strength, however, can avoid such local fluctuations because of enhanced electric body force, leading to smoothened temporal fluctuations in velocity.

Scaling Analysis of Electrothermal Advection. The flow visualization studies show that modulation of the internal advection dynamics by the field leads to reduction of the evaporation rates. Advection in such droplets may be caused by thermal advection or solutal advection, or a combination. Consequently, it is pertinent to deduce which modality of advection is affected by the electric field to its quantitative extent. A scaling analysis is proposed to segregate and quantify the dominant mechanism.[31,35] The analysis is based upon assumptions that thermophysical properties remain invariant, and surface tension only varies because of either thermal or concentration gradients generated within the droplet. The thermophysical properties of the fluid are assumed to be invariant with electric field (as the field strengths are not in the kilovolt range). The energy balance equation applied to the droplet during evaporation correlating the thermal-advection and the internal electrohydrodynamics is expressible as

$$h_{fg}\frac{dm}{dt} = k_{th}A\frac{\Delta T_m}{R} + \rho C_p U_{c,m} A \Delta T_m - \rho C_p V_f A \Delta T_m \qquad (4)$$

The variables dm/dt, h_{fg}, k_{th}, A, ρ, C_p, ΔT_m, $U_{c,m}$, and V_f represent the mass rate of evaporation, the latent heat of vaporization, the thermal conductivity of the fluid, the heat transfer area of the droplet, density and specific heat of the fluid, temperature difference across the interface of the droplet and the droplet bulk, the internal circulation velocity due to thermally driven advection, and internal velocity with electric field-driven advection, respectively. In eq 4, the left-hand side represents the energy flux from the droplet. The right-hand side terms represent the diffusion thermal transport across the droplet, the thermal advection term, and the electrothermal advection term, respectively.

The thermal advection arises because of the difference of temperature across the droplet bulk and interface, which is caused by evaporative cooling.[31] The additional electrothermal component represents the advection due to the internal electrohydrodynamics. The sign of the electrothermal component can be deduced from the fact that the inclusion of electric field weakens the convection current as seen earlier. As it is clearly evident by comparing Figure 6a, (with no field condition) with Figure 6b−e (with the field applied condition), the external field stimuli weaken the strength of internal advective currents. The magnitude of different parts is compared with Figure 6a; a drop is recorded with induction of an electric field. The direction of the internal circulation also changes with the presence of the electric field. The negative sign represents the experimental observation of decrement in evaporation rates in the presence of the field. The assumption is further affirmed in further analysis presented in Figure 8. The thermal gradients generated by the evaporation drive the thermal advection, both within the bulk and at the interface,

caused by the thermal Marangoni effect. However, as the interfacial dynamics cannot be visualized and quantified directly, the effective circulation dynamics at the interface and the bulk can be quantified using the Marangoni number.

The spatially averaged internal circulation velocity due to thermal Marangoni effect is expressed as $U_{c,m} = \sigma_T \Delta T_M / \mu$ as,[31] where σ_T represents the rate of change of surface tension due to change of temperature and μ is the kinematic viscosity of the fluid. The average electrothermal advection velocity V_f is deduced from the force balance of the electrohydrodynamic system within the droplet environment. The solvated ions within the fluid experience motion because of the thermal advection, which in the presence of an electric field gives rise to a modified velocity. For a moving charged entity in the presence of an electromagnetic field, the net force experienced is expressible as

$$\vec{F} = q\vec{E} + (\sigma_e \cdot \vec{E} \times \vec{B}) + \sigma_e(\vec{v} \times \vec{B}) \times \vec{B} \tag{5}$$

where $\vec{F}$, q, $\vec{E}$, $\vec{B}$, $\vec{v}$, and σ_e represent the electromagnetic force, the charge of the ion, the electric field strength, the magnetic field strength, the velocity of the particle, and electrical conductivity of the fluid, respectively. In the case of the present electric field, the strengths are not high enough to induce large enough alternating magnetic fields[35] to affect droplet evaporation. In the case of only an electric field and a negligible magnetic field, eq 5 reduces to

$$\vec{F} = q\vec{E} \tag{6}$$

Considering the volumetric body force, eq 6 can be expressed as

$$f = \rho_e \vec{E} \tag{7}$$

where ρ_e is the charge per unit volume ($=zeN$), f is the electromagnetic force per unit volume, and z, e and, N represent valence of the solvated, the elementary charge magnitude, and the number density of solvated ions in the system. The electrical body force leads to inertial advection within the droplet, which can be expressed as

$$\rho_e E = \rho a \tag{8}$$

where a is an acceleration component because of internal circulation velocity due to the applied external electric field. The acceleration can be scaled as $a \sim V_f / t$ and further, the time elapsed can be scaled as $t \sim R/V_f$, where R is the instantaneous radius of the droplet. Therefore, eq 8 can be expressed as

$$\rho_e E = \rho \frac{V_f^2}{R} \tag{9}$$

From eq 9, the internal circulation velocity in the presence of an electric field stimulus can be expressed as

$$V_f = \sqrt{\frac{\rho_e E R}{\rho}} \tag{10}$$

The product of the electric field and the associated length scale (instantaneous droplet radius) is expressed as the effective electric field potential (V) and eq 10 can be expressed as

$$V_f = \sqrt{\frac{eNzV}{\rho}} = \frac{\nu}{R}\sqrt{\frac{eNzVR^2}{\rho\nu^2}} \tag{11}$$

$$V_f = \frac{\nu}{R}\sqrt{E_{HD}} \tag{12}$$

where ν and E_{HD} represent the kinematic viscosity and the electrohydrodynamic number, respectively. In the concept of the E_{HD}, the role of the field frequency is not inherently defined at steady-state conditions. Hence, an effective V was determined using scaling. The applied alternating voltage, $V'(t) = V_0 \sin(2\pi f t)$, where f is the frequency is integrated over half time period $t/2$, to obtain the area under the signal (essentially the sum of infinite strips of the product of $V'(t)t$ over half the signal wavelength is determined). Next, a rectangular waveform is assumed such that it has an amplitude V and the same frequency f. The area under the signal for the half-time period is thus Vt. The two waveforms are considered analogous, and the areas are equated, which yields the effective voltage V (which includes the component of the frequency of the originally applied signal). This effective voltage is used to deduce the effective E_{HD}. The method is noted to yield accurate predictions of the experimental observations (discussed later).

Substituting the respective expressions for $U_{c,m}$ and V_f in eq 4, and arranging, eq 13 is obtained as

$$\rho \frac{dR}{dt} A h_{fg} = k_{th} A \frac{\Delta T_m}{R} + \rho C_p A \Delta T_m \frac{\sigma_T \Delta T_m}{\mu} - \rho C_{fp} A \Delta T_m \frac{\nu}{R}\sqrt{E_{HD}} \tag{13}$$

$$\rho \frac{dR}{dt} R h_{fg} = k_{th} \Delta T_m \left[1 + \rho C_p \frac{R\sigma_T \Delta T_m}{k_{th}\mu} - \rho C_{pf} \frac{\nu}{k_{th}}\sqrt{E_{HD}} \right] \tag{14}$$

$$\rho \frac{dR}{dt} R h_{fg} = k_{th} \Delta T_m [1 + Ma_T - Pr\sqrt{E_{HD}}] \tag{15}$$

where dR/dt, Pr, and Ma_T represent the rate of change of equivalent radius of the droplet, Prandtl number, and thermal Marangoni number, respectively. For stable internal advection, $Ma_T \gg 1$,[31] and eq 15 can be scaled as

$$\rho \frac{dR}{dt} R h_{fg} \approx k_{th} \Delta T_m [Ma_T - Pr\sqrt{E_{HD}}] \tag{16}$$

In eq 16, the term $(Pr\sqrt{E_{HD}})$ represents the effect of the electric field on the thermal diffusion within the droplet and is termed as the electro-Prandtl number, and as observed front the eq 16, it acts as a deterrent to the thermal Marangoni advection dynamics (represented by the thermal Ma). The whole term $(Ma_T - Pr\sqrt{E_{HD}})$ is termed as the effective electrothermal Marangoni number ($Ma_{T,e}$), and its modulus value determines the strength of electroadvection within the droplet. The extent of deterioration in internal velocity depends on the magnitude of the electro-Prandtl number, which is a direct function of the field parameters.

Figure 8 illustrates the contribution of a different mechanism in thermal and species transport with variant frequency and field strength. The individual components of thermal transport were calculated from eq 13. Figure 8a,b illustrate the contributions to the thermal transport by the convection and electroadvection components. The thermal diffusion component is very small ($\sim$1−2%) and has not been illustrated. At zero-field condition, $\sim$100% of the thermal transport contribution comes from the convection term. With the

application of the field, the electroadvection component (marked as electric in the figure) increases and the convective component reduces. In those cases, where the magnitudes are similar, the internal advection is nearly seized. Hence, this is in accordance with our assumption that the internal advective currents due to thermal Marangoni are in the opposite direction to that of the electrothermal advection because of the application of the electric field. In the event that the electric component overshoots the convective one, the internal advection further improves; however, this is caused predominantly by the electroadvection rather than the thermal convection. From Figure 8a,b it can be further observed that the effect of field strength is more prominent than the effect of frequency. Figure 8c,d illustrates the similar contributions to species transport due to solutal advection and the electrosolutal components, and these shall be discussed in upcoming sections. The possibility that thermal gradients within the droplet lead to circulation because of Rayleigh convection also exists and its potential vis-à-vis the Marangoni convection must also be established.

The internal circulation velocity, if induced by the buoyancy effect, can be expressed as $u = g\beta\Delta T_R R^2/\nu$,[31] where g, β, and ΔT_R are acceleration due to gravity, the thermal expansion coefficient of the fluid, and the temperature difference within the droplet because of which the buoyancy advection effect might arise. The temperature difference arises because of evaporative cooling, may lead to the Rayleigh convection, and can be expressed as[14,31]

$$\Delta T_R = \sqrt{\frac{\nu h_{fg}}{g\beta R^2 C_P}\frac{dR}{dt}} \tag{17}$$

The associated Rayleigh number is expressed as

$$Ra = \frac{R^2}{\alpha}\sqrt{\frac{h_{fg}g\beta}{C_P\nu}\frac{dR}{dt}} \tag{18}$$

However, the contribution of buoyancy-driven circulation in the evaporation process is negligible as compared to Marangoni convection, and this has been confirmed in the literature.[31,35] Additionally, it is of importance to determine if the circulation patterns within the droplet are temporally stable or are, in general, intermittent. This can be determined from the stability criteria[36,37] represented in the form of a summation of two ratios, Ra/Ra_c and Ma/Ma_c. The Ra_c and Ma_c are the critical Ra and critical thermal Ma. The ratio Ra/Ra_c presents the extent of thermal Rayleigh advection relative to its possible maxima within the droplet and Ma/Ma_c depicts the same for the thermal Marangoni advection. The criteria for temporally stable circulation is

$$\frac{Ra}{Ra_c} + \frac{Ma}{Ma_c} = 1 \tag{19}$$

The Ma_T and Ra values have been plotted for variations in frequency and field strength in Figure 9a,b, respectively. From the analysis of Nield[36] and Davis,[37] the values of the Ma_c are ~81 and ~53, respectively. Ra_c is the criterion for onset of thermal buoyant convection at ~1708 from Chandrasekhar's classical stability analysis. These end coordinates and eq 19 are used to construct the stability lines in Figure 9. The addition of salt results in shifting of the points toward the right and upward on the Ma_T versus Ra plot compared to the pure water case. The zero field cases show marginally stable circulation
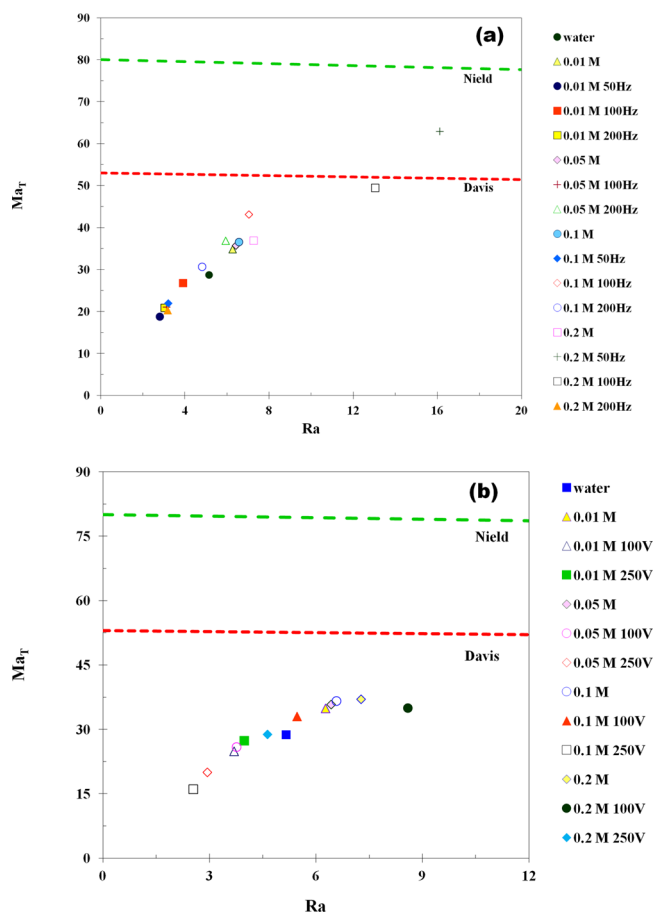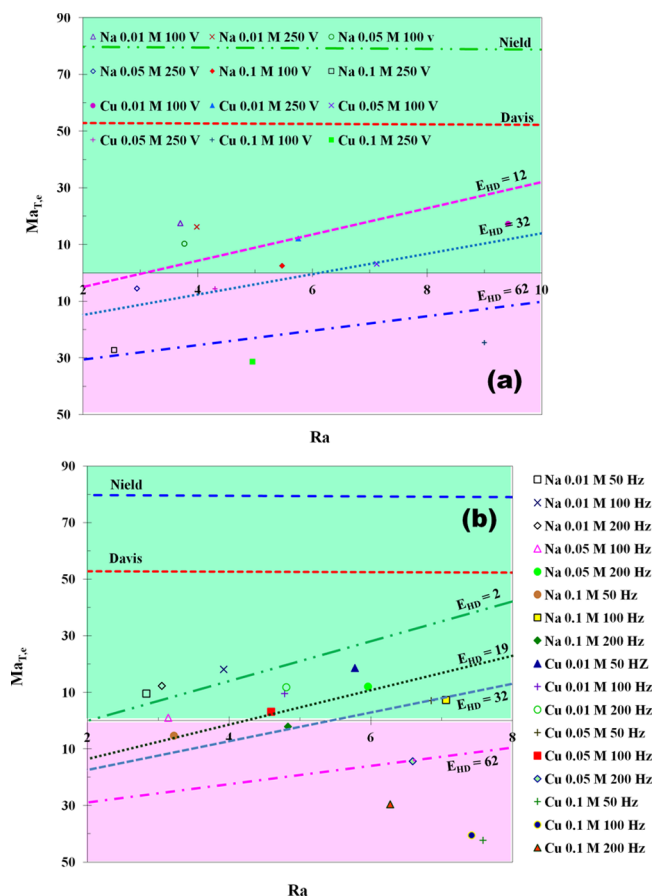

Figure 9. Stability plot for thermal Ma with the respect to Ra to determine the nature of temporal stability of internal circulation (a) with a variation of frequency and salt concentration (b) with a variation of field strength and salt concentration.

(lies between the two stability criteria lines), which enhances evaporation compared to water. With the input stimulus of different frequencies (Figure 9a) at 150 V, the points are observed to shift downward and below the region of stable circulation ubiquitously. This justifies the decreased velocity of circulation observed in the case of field-influenced evaporating droplets during flow visualization. Several cases also drop below the water case, which signifies that the thermal Ma effect is largely suppressed by the electric field and as observed before, higher frequencies lead to lower degrees of arrest compared to lower frequencies. For variation of field strength (Figure 9b) at 100 Hz, all points lie within the criteria of unstable circulation, and in comparison to Figure 9a, the thermal Ma values are further lowered. This reveals that the field strength has a domineering role over frequency in diminishing internal circulation because of thermal advection, and it is in accordance with the visualization results.

A similar stability plot representing the effective electrothermal Ma ($Ma_{T,e}$) and Ra has been illustrated in Figure 10. Figure 10a illustrates the variation of frequency and has been segregated into two regimes. The green region represents the condition where the thermal Ma is greater than the electro-Prandtl number ($Ma_T > Pr\sqrt{E_{HD}}$), whereas the pink region represents ($Ma_T < Pr\sqrt{E_{HD}}$). For stable circulation to exist, the points should cross the stability lines (not shown in pink regions) in the corresponding region. Iso-E_{HD} lines have been

Figure 10. Stability plot for electrothermal Ma vs Ra (a) with a variation of field strength and concentration (b) with frequency and concentration variation. The iso-E_{HD} lines represent the shift of the points of stability under variant field conditions.

illustrated in Figure 10, which show the variation and trend of internal circulation kinetics for known values of E_{HD}. It is observed that all the points in Figure 10a,b are further shifted downward and leftward on the map (in comparison to their locations on Figure 9), which signifies that the effective electrothermal Ma is the main modulating factor for the thermal advection within the droplet. It is noteworthy that several cases, such as CuSO$_4$ 0.05 M at 100 V and NaI 0.05 M at 250 V, exhibit very similar circulation velocities in the visualization studies, but their positions on Figure 10a with respect to the $Ma_{T,e}$ are quite different.

Whereas the CuSO$_4$ case lies in the green region, the NaI case lies in the pink zone. This provides an interesting insight into the electrohydrodynamics of the problem at hand. Although both droplets exhibit similar internal advection velocity and similar evaporation dynamics (of course, NaI has to be at a higher field strength as its zero-field advection is stronger[14]), the CuSO$_4$ case undergoes internal advection by virtue of superior thermal Marangoni advection, whereas the NaI case experiences circulation because of a superior electro-Prandtl component of advection. This essentially signifies that the reduction of evaporation is due to competitive electro-thermal and thermal Marangoni advection. In the event that the electrothermal component largely exceeds the thermal Ma component, it can lead to the large value of $Ma_{T,e}$ in the pink region, which will give rise to augmented circulation, whose stability will be determined from the criteria by Davis and Nield in the pink region (not illustrated). The iso-E_{HD} lines provide further insight into the problem. Assume that a saline droplet exhibits circulation and lies somewhere near the Davis line (Figure 10) at zero-field. At a constant Ra, if the E_{HD} is enhanced for a saline solution (by improving the field strength), the value of $Ma_{T,e}$ will deteriorate to zero, with a decrease in circulation and the evaporation rate. With further increase of the field strength, the electro-Prandtl number overshadows the thermal Ma, causing the absolute value of the $Ma_{T,e}$ to increase once more, leading to increased circulation (because of electroadvection) and increased evaporation rate. Similar instances are observable from Figure 10a,b.

Scaling Analysis of Electrosolutal Advection. Although a detailed analysis and discussion on the role of electrothermal advection has been presented, literature shows that saline droplets exhibit enhanced evaporation because of the dominant solutal advection over the thermal one;[14] therefore, the possible role of the electrosolutal advection must also be analyzed. As the evaporation of the droplet with solvated ions progresses, only fluid molecules depart with time, thereby enhancing the bulk concentration of solvated ions as the process continues. However, it is noteworthy that the fluid molecules depart only from the interface, which leads to localized enhanced solute concentration at the droplet interface in comparison to the bulk of the droplet. This concentration gradient leads to a solutal component advection within the droplet. The interface also experiences solutal Marangoni advection caused by the concentration gradient along with the droplet interface (because of the inherent difference in evaporation created by the very geometry of the pendant shape).[14,31] The quantification of evolving bulk
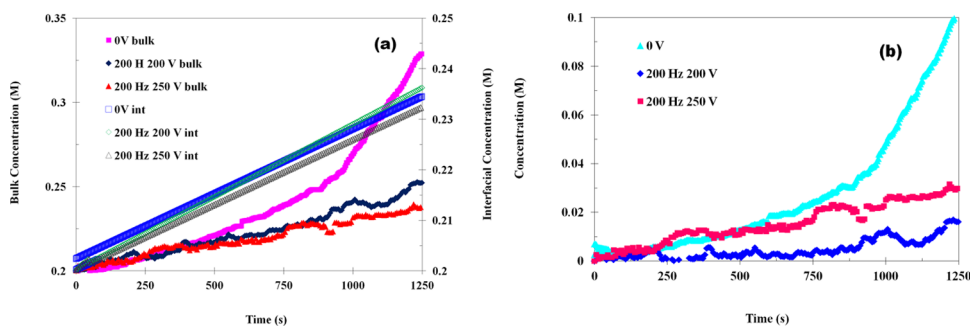
Figure 11. (a) Dynamic and bulk concentration within the droplet (0.2 M NaI) as evaporation evolves. The "*int*" represents the dynamic surface or interfacial concentration and "*bulk*" represents the dynamic bulk concentration. The bulk concentration has been plotted on the left-hand ordinate and the interfacial concentration on the right-hand ordinate. (b) Concentration difference for cases corresponding to (a).
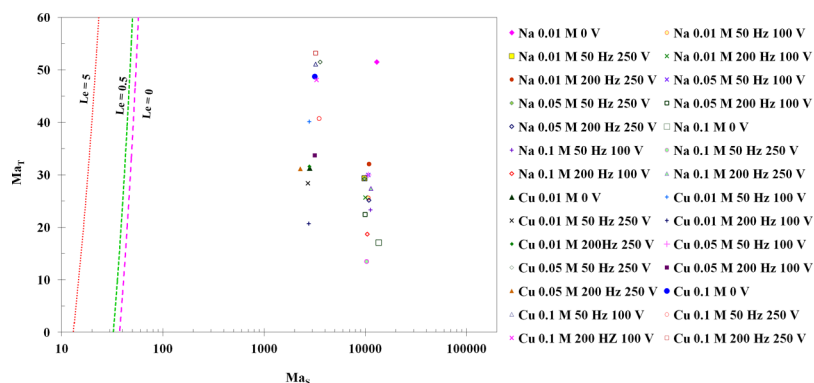
Figure 12. Phase map of the thermal Ma against the solutal Ma under variant field constraints. The iso-Le lines are adapted from literature.[39]

concentration is achieved from total species conservation (CV_t = constant, where V_t and C represent the instantaneous volume and dynamic bulk concentration). For mapping the dynamic interfacial concentration, initially, the relationship between the surface tension concerning the concentration is determined.[35] Further, the instantaneous surface tension of the droplet is mapped as the evaporation process evolves via pendant drop shape tensiometry analysis. Correlating the instantaneous surface tension with the concentration relation yields the dynamic evolution of the interfacial concentration. The exercise is done only for the initial 15−20 min of the evaporation process. Beyond this, the Worthington number (Wo) of the droplet ($Wo = V_{inst}/V_0$, where V is the droplet volume and subscripts inst and 0 represent instantaneous and initial conditions) reduces below ∼0.75, and further determination of surface tension by drop shape analysis will be erroneous.[38] The maximum volume can be expressed as $V_{max} = \pi D_n \gamma/\Delta \rho g$ where D_n is the needle diameter, γ is the surface tension of the test fluid, and ρ is the density. Hence, this can be further expressed as $Wo = \Delta \rho g V_d/\pi \gamma D_n$. Therefore, the Worthington number is basically the bond number with the length scale as $\sqrt{\frac{V_d}{\pi D_n}}$. Figure 11a illustrates the dynamic bulk and interfacial concentrations for the NaI solution droplet (0.2 M) in case of variant electric field constraints. The deviation in interfacial concentration is insignificant among the different cases; however, in the case of bulk concentration, the change is noticeably high. The concentration difference (ΔC) (Figure 11b) decreases in the presence of the electric field compared to the 0 V case. This concentration gradient within the droplet drives the solutal advection during the evaporation process.

Thereby, it is evident that the presence of the electric field leads to a reduction in the concentration gradient, which signifies a reduction in the solutal advection within the droplet. To quantify the effect of electrosolutal advection on the evaporation kinetics, species conservation is applied as

$$\frac{dm}{dt} = DA\frac{\Delta C_m}{R} + U_{c,m}\Delta C_m A - V_{f,c}\Delta C_m A \qquad (20)$$

where dm/dt, D, and ΔC_m are the mass rate of evaporation, the diffusion coefficient of the solute in the fluid, and the driving concentration gradient within the droplet (the difference between dynamic bulk and interfacial concentrations). $U_{c,m}$ and $V_{f,c}$ represent the internal circulation velocity driven by the solutal gradient at zero-field and the electrosolutal advection velocity in the electric field environment. Similar to internal circulation velocity due to thermal gradient, $U_{c,m} = \sigma_c \Delta C_m/\mu$,

where σ_c is the rate of change of surface tension with respect to change in the solutal concentration.[14] Substituting the expressions for velocities in eq 20, the expression yields

$$\rho\frac{dR}{dt}R = D\Delta C_m + \frac{\sigma_c(\Delta C_m)^2 R}{\mu} - \nu(\sqrt{E_{HD}})\Delta C_m \qquad (21)$$

$$\frac{\rho R}{D\Delta C_m}\frac{dR}{dt} = (1 + Ma_s - Sc\sqrt{E_{HD}}) \qquad (22)$$

where Ma_s and Sc are the solutal Marangoni number and Schmidt number. The term ($Sc\sqrt{E_{HD}}$) represents the electro-solutal convection contribution due to the electric field. Rearranging eq 21 and putting $Ma_s \gg 1$[31]

$$\frac{\rho R}{D\Delta C_m}\frac{dR}{dt} \approx Ma_s - \sqrt{Sc_{sp}}\sqrt{E_{HD}Sc_i} \qquad (23)$$

where $\sqrt{Sc_{sp}}$ represents the species transport Schmidt number and $\sqrt{E_{HD}Sc_i}$ represents the electro-Schmidt number (Sc), where Sc_i is the ionic Sc, which is the ratio of mobility (m) to the diffusivity of the solvated ions($Sc_i = m_{ion}/D_{ion}$). The term ($Ma_s - \sqrt{Sc_{sp}}\sqrt{E_{HD}Sc_i}$) behaves as the effective electrosolutal Ma for the system. The electro-Schmidt number essentially indicates the extent of ionic absorption−desorption at the droplet interface due to the applied electric field and its consequences on the internal and interfacial advection dynamics. Figure 12 illustrates the stability plot for the thermal Ma with respect to the solutal Ma (Ma_T vs Ma_s). Iso-Lewis number lines, proposed by Joo (1995), have been used to estimate the stability and behavior of the internal advection. All the points are found to lie toward the right side of the $Le = 0$ line, with large values of the Ma_s compared to the Ma_t, signifying the dominant nature of the solutal Marangoni advection over the thermal Marangoni within the droplet.[14,31] However, the traditional stability map of the Ma_t and Ma_s is insufficient to determine the effects of electrosolutal effects as it is observed that hardly any difference in the Ma_s can be observed under field constraints, thereby making the deduction of electrosolutal effects difficult. Figure 13 illustrates the effective thermal Marangoni number ($Ma_{T,e}$) and effective solutal Marangoni number ($Ma_{s,e}$) for variations in field frequency and strength. Similar to Figure 10, two regions have been mapped depending on the dominating mechanism contributing to $Ma_{T,e}$. In the present case, the field strengths are not potent enough to lead to($Ma_s < Sc\sqrt{E_{HD}}$). It is observed that with an increase in the electric field frequency or
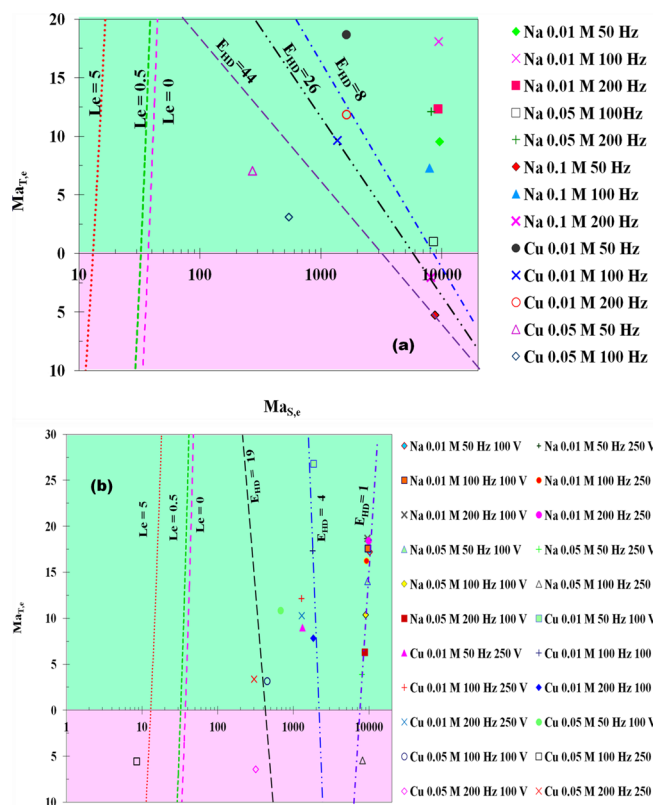
Figure 13. Map of the effective electrothermal Ma against the effective electrosolutal Ma for (a) frequency variation at 100 V and (b) voltage variation. The regimes are represented by the different iso-Le lines[39] and the iso-E_{HD} lines.

strength, the points shift toward the origin, indicating a reduction in the solutal advection component as well as the thermal component. The direction of the shift with increasing field parameters is evident from the behavior of the iso-E_{HD} lines, where the points shift nearer to the origin with an increase in field parameters. However, it is evident that the relative decrease in the value of the $Ma_{s,e}$ is comparatively larger than the reduction in the $Ma_{T,e}$. This indicates that the opposing electrosolutal advection is the dominant mechanism governing the retarded evaporation kinetics of ionic fluids under various external electric field stimuli. The arrested thermal advection by the opposing electrothermal advection plays the recessive role. As the effective electrosolutal Ma is revealed as the dominant governing parameter, the modified circulation velocity under field effect is inversely deduced from eq 20. Representative theoretical velocities are illustrated in Figure 7b and a good match is observed with respect to the corresponding spatially averaged circulation velocities. This further cements the finding that the electrosolutal dynamics is the dominant governing mechanism responsible for seized evaporation.

CONCLUSIONS

The present article reports experimentally observed reduction in evaporation rates of pendant droplets with solvated ions under the influence of an alternating electric field. The evaporation kinetics is analyzed to conform to the classical D^2 law and extended to different field strengths and frequencies of various saline fluids. The rate of evaporation is found to deteriorate even below the evaporation rate of a pure water

droplet with an increase in field strength. The field frequency is observed to improve the evaporation rates; however, it remains less than the zero-field condition. The observation has been explained based on the solvation characteristics of the ions. The change in surface tension due to interfacial adsorption is evaluated to determine the root cause, however, it is observed to be insufficient to explain the kinetics. Next, the classical diffusion-driven evaporation model is appealed to, and it is found to fall short in predicting the observed evaporation rates. The role of the internal hydrodynamics is then probed into, and PIV reveals a consistent reduction in the internal advection velocity within the droplet under the influence of the electric field. Additionally, change in the orientation of the internal circulation dynamics is also observed and has been explained based on electrohydrodynamic considerations. The flow visualization reveals that internal advection dynamics could be a responsible agent for the anomalous evaporation rates.

A scaling model is proposed to determine the roles of the thermal and the solutal modes of advection on the internal advection. The thermal scaling model presents the inability of the thermal Marangoni and Rayleigh convection models to capture the internal advection dynamics. It is deduced that the effective electrothermal Marangoni convection is a governing parameter and the electrodiffusive advection (represented by the electro-Prandtl number) is responsible for the seizure of the thermal advection. Further, the role of solutal advection is modeled, and the analysis reveals that the electrosolutal Ma governs the effective advection kinetics. In the solutal advection, the electrosolutal advection (represented by the electro-Schmidt number) opposes the solutal advection (represented by the solutal Ma), leading to retarded internal circulation. Stability mapping of the electrothermal and electrosolutal effects reveals that with increasing E_{HD}, the effective solutal advection decays dominantly compared to the decay of the effective electrothermal advection. Further, the theoretical velocities derived from the electrosolutal model corroborate well with the PIV observations, thereby establishing the electrosolutal effect as the governing mechanism behind the suppressed evaporation rate. The observations show that the directionality of the electric field may lead to suppressed evaporation as well as aided behavior.[40,41] The findings on the competitive electrohydrodynamics and electrosolutal effects in solvated ion droplets may find strong implications in microscale electrohydrodynamic and thermofluidic transport systems.

AUTHOR INFORMATION

Corresponding Author

Purbarun Dhar — Department of Mechanical Engineering, Indian Institute of Technology Kharagpur, Kharagpur 721302, West Bengal, India; ⊙ orcid.org/0000-0001-5473-2993; Phone: +91-3222-28-2938; Email: purbarun@mech.iitkgp.ac.in, purbarun.iit@gmail.com

Authors

Vivek Jaiswal — Department of Mechanical Engineering, Indian Institute of Technology Ropar, Rupnagar 140001, Punjab, India

Shubham Singh — Department of Mechanical Engineering, Indian Institute of Technology Ropar, Rupnagar 140001, Punjab, India

Anilakkad Raman Harikrishnan − *Department of Mechanical Engineering, Birla Institute of Technology and Science Pilani, Pilani 333031, Rajasthan, India*

Complete contact information is available at:
https://pubs.acs.org/10.1021/acs.langmuir.0c01619

Notes

The authors declare no competing financial interest.

■ ACKNOWLEDGMENTS

■ REFERENCES

(1) Chiang, C. H.; Raju, M. S.; Sirignano, W. A. Numerical analysis of convecting, vaporizing fuel droplet with variable properties. *Int. J. Heat Mass Transfer* **1992**, *35*, 1307−1324.

(2) Faeth, G. M. Evaporation and combustion of sprays. *Prog. Energy Combust. Sci.* **1983**, *9*, 1−76.

(3) Abramzon, B.; Sirignano, W. A. Droplet vaporization model for spray combustion calculations. *Int. J. Heat Mass Transfer* **1989**, *32*, 1605−1618.

(4) Hu, H.; Larson, R. G. Analysis of the effects of Marangoni stresses on the microflow in an evaporating sessile droplet. *Langmuir* **2005**, *21*, 3972−3980.

(5) Jing, J.; Reed, J.; Huang, J.; Hu, X.; Clarke, V.; Edington, J.; Housman, D.; Anantharaman, T. S.; Huff, E. J.; Mishra, B.; Porter, B.; Shenker, A.; Wolfson, E.; Hiort, C.; Kantor, R.; Aston, C.; Schwartz, D. C. Automated high resolution optical mapping using arrayed, fluid-fixed DNA molecules. *Proc. Natl. Acad. Sci.* **1998**, *95*, 8046−8051.

(6) Kawase, T.; Sirringhaus, H.; Friend, R. H.; Shimoda, T. Inkjet Printed Via-Hole Interconnections and Resistors for All-Polymer Transistor Circuits. *Adv. Mater.* **2001**, *13*, 1601−1605.

(7) Picknett, R. G.; Bexon, R. The evaporation of sessile or pendant drops in still air. *J. Colloid Interface Sci.* **1977**, *61*, 336−350.

(8) Kaushal, A.; Jaiswal, V.; Mehandia, V.; Dhar, P. Soluto-thermo-hydrodynamics influenced evaporation kinetics of saline sessile droplets. *Eur. J. Mech. B Fluids* **2020**, *83*, 130−140.

(9) Semenov, S.; Trybala, A.; Agogo, H.; Kovalchuk, N.; Ortega, F.; Rubio, R. G.; Starov, V. M.; Velarde, M. G. Evaporation of droplets of surfactant solutions. *Langmuir* **2013**, *29*, 10028−10036.

(10) Godsave, G. A. E. Studies of the combustion of drops in a fuel spray- The burning of single drops of fuel. *Symp. (Int.) Combust.* **1953**, *4*, 818−830.

(11) Kuz, V. A. Fluid dynamic analysis of droplet evaporation. *Langmuir* **1992**, *8*, 2829−2831.

(12) Dhar, P.; Jaiswal, V.; Harikrishnan, A. R. Electromagnetic field orientation and characteristics governed hydrodynamics within pendent droplets. *Phys. Rev. E* **2018**, *98*, 063103.

(13) Rossow, V. J. *On Flow of Electrically Conducting Fluids Over a Flat Plate in the Presence of a Transverse Magnetic Field, Report 1358−Nat*; Advisory Committee for Aeronautics, 1958; pp 489−508.report

(14) Jaiswal, V.; Harikrishnan, A. R.; Khurana, G.; Dhar, P. Ionic solubility and solutal advection governed augmented evaporation kinetics of salt solution pendant droplets. *Phys. Fluids* **2018**, *30*, 012113.

(15) Bateni, A.; Ababneh, A.; Elliott, J. A. W.; Neumann, A. W.; Amirfazli, A. Effect of gravity and electric field on shape and surface tension of drops. *Adv. Space Res.* **2005**, *36*, 64−69.

(16) Bateni, A.; Laughton, S.; Tavana, H.; Susnar, S. S.; Amirfazli, A.; Neumann, A. W. Effect of electric fields on contact angle and surface tension of drops. *J. Colloid Interface Sci.* **2005**, *283*, 215−222.

(17) Dhar, P. Thermofluidic transport in droplets under electro-magnetic stimulus: A comprehensive review. *J. Indian Inst. Sci.* **2019**, *99*, 105−119.

(18) Reznik, S. N.; Yarin, A. L.; Theron, A.; Zussman, E. Transient and steady shapes of droplets attached to a surface in a strong electric field. *J. Fluid Mech.* **2004**, *516*, 349−377.

(19) Basaran, O. A.; Wohlhuter, F. K. Effect of nonlinear polarization on shapes and stability of pendant and sessile drops in an electric (magnetic) field. *J. Fluid Mech.* **1992**, *244*, 1−16.

(20) Miksis, M. J. Shape of a drop in an electric field. *Phys. Fluids* **1981**, *24*, 1967−1972.

(21) Adamiak, K. Interaction of two dielectric or conducting droplets aligned in the uniform electric field. *J. Electrost.* **2001**, *51−52*, 578−584.

(22) Digilov, R. Charge-induced modification of contact angle: the secondary electrocapillary effect. *Langmuir* **2000**, *16*, 6719−6723.

(23) Kang, K. H. How electrostatic fields change contact angle in electrowetting. *Langmuir* **2002**, *18*, 10318−10322.

(24) Mugele, F.; Baret, J.-C. Electrowetting: from basics to applications. *J. Phys.: Condens. Matter* **2005**, *17*, R705−R774.

(25) Celestini, F.; Kirstetter, G. Effect of an electric field on a Leidenfrost droplet. *Soft Matter* **2012**, *8*, 5992−5995.

(26) Gunji, M.; Washizu, M. Self-propulsion of a water droplet in an electric field. *J. Phys. D: Appl. Phys.* **2005**, *38*, 2417.

(27) Hase, M.; Watanabe, S. N.; Yoshikawa, K. Rhythmic motion of a droplet under a dc electric field. *Phys. Rev. E: Stat., Nonlinear, Soft Matter Phys.* **2006**, *74*, 046301.

(28) Kim, H.; Luo, D.; Link, D.; Weitz, D. A.; Marquez, M.; Cheng, Z. Controlled production of emulsion drops using an electric field in a flow-focusing microfluidic device. *Appl. Phys. Lett.* **2007**, *91*, 133106.

(29) Chabert, M.; Dorfman, K. D.; Viovy, J.-L. Droplet fusion by alternating current (AC) field electrocoalescence in microchannels. *Electrophoresis* **2005**, *26*, 3706−3715.

(30) Jayasinghe, S. N.; Qureshi, A. N.; Eagles, P. A. M. Electrohydrodynamic jet processing: an advanced electric-field-driven jetting phenomenon for processing living cells. *Small* **2006**, *2*, 216−219.

(31) Mandal, D. K.; Bakshi, S. Internal circulation in a single droplet evaporating in a closed chamber. *Int. J. Multiphase Flow* **2012**, *42*, 42−51.

(32) Charlesworth, D. H.; Marshall, W. R., Jr. Evaporation from drops containing dissolved solids. *AIChE J.* **1960**, *6*, 9−23.

(33) Masunov, A.; Dannenberg, J. J.; Contreras, R. H. C− H Bond-Shortening upon Hydrogen Bond Formation: Influence of an Electric Field. *J. Phys. Chem. A* **2001**, *105*, 4737−4740.

(34) Valderrama, J. O.; Campusano, R. A.; Forero, L. A. A new generalized Henry-Setschenow equation for predicting the solubility of air gases (oxygen, nitrogen and argon) in seawater and saline solutions. *J. Mol. Liq.* **2016**, *222*, 1218−1227.

(35) Jaiswal, V.; Dwivedi, R. K.; Harikrishnan, A. R.; Dhar, P. Magnetohydrodynamics and magneto-solutal transport mediated evaporation dynamics in paramagnetic pendent droplets under field stimulus. *Phys. Rev. E* **2018**, *98*, 013109.

(36) Nield, D. A. Surface tension and buoyancy effects in the cellular convection of an electrically conducting liquid in a magnetic field. *Z. Angew. Math. Phys.* **1966**, *17*, 131−139.

(37) Davis, S. H. Buoyancy-surface tension instability by the method of energy. *J. Fluid Mech.* **1969**, *39*, 347−359.

(38) Harikrishnan, A. R.; Dhar, P.; Gedupudi, S.; Das, S. K. Oscillatory solutothermal convection-driven evaporation kinetics in colloidal nanoparticle-surfactant complex fluid pendant droplets. *Phys. Rev. Fluid.* **2018**, *3*, 073604.

(39) Joo, S. W. Marangoni instabilities in liquid mixtures with Soret effects. *J. Fluid Mech.* **1995**, *293*, 127−145.

(40) Jaiswal, V.; Dhar, P. Interplay of electro-thermo-solutal advection and internal electrohydrodynamics governed enhanced evaporation of droplets. *Proc. R. Soc. A* **2019**, *475*, 20190046.

(41) Harikrishnan, A. R.; Dhar, P. Optical thermogeneration induced enhanced evaporation kinetics in pendant nanofluid droplets. *Int. J. Heat Mass Transfer* **2018**, *118*, 1169−1179.